14,12

Effect of proton and gamma radiation on a polymer composite

© V.I. Pavlenko[1], A.V. Noskov[2], R.V. Sidelnikov[1,¶], V.A. Shurshakov[3], V.V. Kashibadze[1], A.Yu. Ruchiy[1]

[1] Belgorod State Technology University named after V.G. Shukhov,
Belgorod, Russia
[2] Belgorod National Research University,
Belgorod, Russia
[3] Institute of Biomedical Problems, Russian Academy of Sciences,
Moscow, Russia

¶ E-mail: roman.sidelnikov@mail.ru

The results of a study of a polymer composite material that can be used as a material for long-term protection of astronauts from radiation exposure in space are presented. The calculation of the linear attenuation coefficient of gamma quanta has been carried out. At the energy of gamma quanta $E = 0.08$ MeV the value of the linear attenuation coefficient is 490.62 cm^{-1}, and at the energy $E = 1.252$ MeV the coefficient is only 0.26 cm^{-1}. The results of the experimental effect of proton radiation on the polymer composite under study are presented. Irradiation was carried out with a proton beam at the phasotron of the Joint Institute for Nuclear Research (JINR), Dubna. During irradiation, we additionally used an aluminum plate 4 mm thick, polyethylene 5 cm thick, and a water absorber of different sizes. The values of absorbed (D_{ETD} (H_2O) $= 17 \pm 1$ mGy) and equivalent dose (H_{ETD} (H_2O) $= 239 \pm 7$ mSv) of secondary particles behind local protection made of a polymer composite were calculated.

Keywords: polymer composite, protection from cosmic radiation, linear attenuation coefficient of gamma quanta, irradiation with a proton beam.

1. Introduction

For space program development, methods, equipment and materials shall be designed to ensure reliable protection of astronauts against adverse space factors with cosmic radiation being one of the most dangerous among them [1,2]. It contains galactic cosmic radiation consisting of continuous isotropic flux of high-energy protons and heavy ions (90% of simple protons, 9% of α-particles and 1% of other heavy ions such as iron (Fe), oxygen (O), neon (Ne), carbon (C), magnesium (Mg) and silicon (Si)) arriving from beyond the Solar system, and solar particles which are sporadic high-energy proton pulses [3,4]. It was pointed out in [5] that, during solar flares, gamma radiation shall be also considered. The recorded maximum gamma quantum energy of solar flares is equal to 300 MeV, and the radiation dose rate is about $2 \cdot 10^{-6}$ J/s that is equal to $3.4 \cdot 10^{-6}$ Rem/s [5]. Neutron background inside spacecraft in the form of secondary radiation due to interaction between galactic cosmic radiation and solar cosmic beams, and between protons trapped in Van Allen belts and chemical element nuclei constituting the Earth's upper atmosphere and of the orbital station materials also poses a threat for astronauts [6,7].

Aluminum and polyethylene are currently the main structural materials for space exploration, but multiple investigations, including simulation and exploration missions, show that these materials do not ensure sufficient protection

against cosmic radiation, therefore, either replacement or installation of additional protection is required [8–11]. Possible installation of additional protection made from aqueous materials was investigated at the Russian segment of the ISS, where „Protective Shutter" was assembled. The average thickness of such protection is 6.3 g/cm^2. Then, using the combination of passive detectors, an average absorbed dose and equivalent dose rate behind and on the side of the protective shutter was recorded. The readings for unprotected areas were $327 \, \mu$Gy/day and $821 \, \mu$Sv/day, and for protected areas — $224 \, \mu$Gy/day and $575 \, \mu$Sv/day, respectively [12]. This suggests that additional protection may be used, but to ensure efficient use on spacecraft, the effective volume occupied by such protection and radiation protection in a wide energy range shall be considered.

There are numerous solutions that may be used in future on board spacecraft to ensure protection against cosmic radiation [13,14]. Immediately before use, each of them needs to be checked by simulation of cosmic radiation transmission through these materials and by experimental exposure to adverse cosmic factors [15]. For example, there is a study focused on protection against neutron cosmic radiation using polymer composite based on epoxy matrix reinforced with polyethylene, carbon and basalt fiber, and WO_3 and BC_4 as fillers. Simulation using the Monte Carlo method was conducted to study the protection against neutron radiation. Boron compound was found to be critical for protection against thermal neutrons, and protection
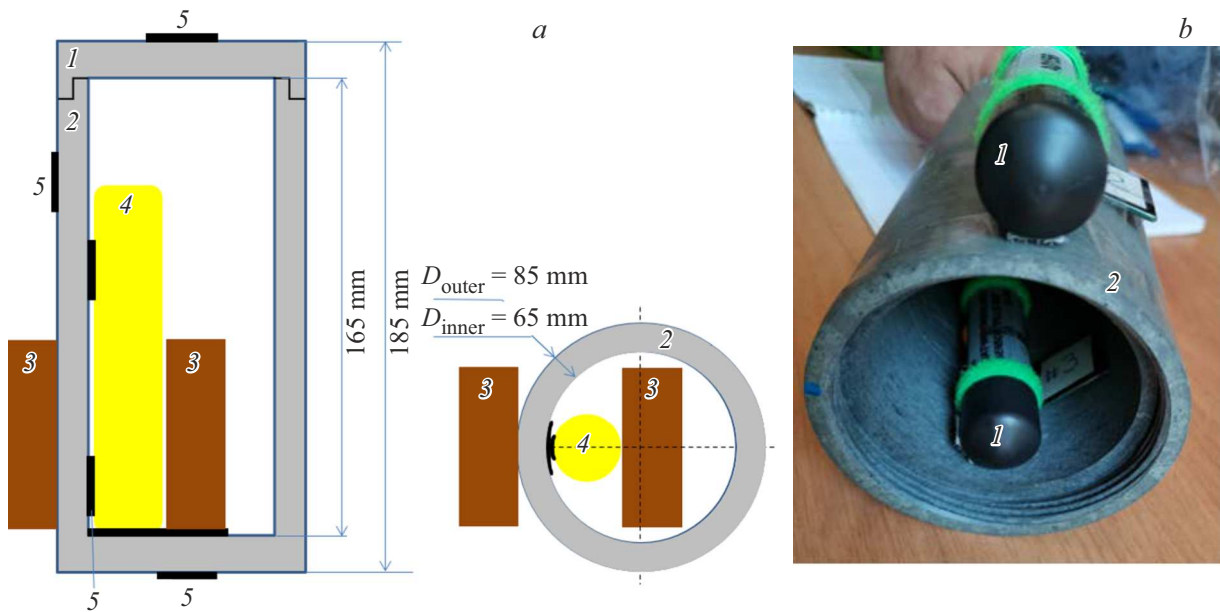
Figure 1. Radiation shutter in the form of container with sensors: *a* — structural model: *1* — container cover, *2* — container body, *3* — passive thermoluminescent and solid state track detector assemblies, *4* — „PILLE-MKS“, detector *5* — „Velcro“ fastener; *b* — photo of a polymer composite container used for irradiation on the synchrotron: *1* — „PILLE-MKS“ detector, *2* — container.

efficiency against fast neutrons primarily depends on the type of fiber. Low weight is the main advantage of this material [16]. But in pursuit of improvement of neutron protective properties, other required properties to be used in space have not been investigated.

An interesting study [17] was carried out where the Geant4 Monte Carlo method was used to simulate transmission of Fe ions with energies 500 MeV/n, 1 GeV/n and 2 GeV/n through multiple materials to study their shielding properties. $^6Li^{10}BH_4$ has been found to be the most efficient hydrogen-containing material from those under study due to reduction of radiation dose higher than that of polyethylene by 20%. It should be noted that carbon fiber-reinforced plastic ensures reduction of radiation dose by a factor of 1.9 compared with aluminum, while having also high mechanical strength. This study confirms that there are many materials that can be used for protection against cosmic radiation instead of the existing materials, but even their introduction will not ensure such protection level that allows long-term space missions.

Results of investigation of polymer composite for protection against cosmic radiation are described herein. Its physical and mechanical properties were studied and experimental data of protection against gamma and proton radiation were provided.

2. Materials and research techniques

2.1. Composite under study

BSTU named after V.G. Shukhov together with Gagarin Research and Test Cosmonaut Training Center has devel-

Table 1. Atomic chemical analysis of protective polymer composite

	Element				
	Bi	O	C	F	W
Concentration in the composite,mass%	52.47	6.03	9.42	29.26	2.82

N o t e. For more detailed description of the analysis and synthesis of the composite, see [18].

oped a polymer composite material suitable for long-term protection of astronauts against radiation exposure in space. Polymer composite is a fluoroplastic matrix with modified radiation protective fillers. Chemical atomic analysis of the material is shown in Table 1.

2.2. Composite exposure to protons

The polymer composite was exposed to a proton beam using a synchrotron of Joint Institute for Nuclear Research (JINR), Dubna. For irradiation, a 4 mm aluminum plate, 5 mm polyethylene, water absorber of different sizes were used additionally. For irradiation, a cylinder was made from the polymer composite of interest, the cylinder (container) design is shown in Figure 1.

The irradiation set up is shown in Figure 2.

For absorbed dose measurement, passive sensors were used — TD-1/HARZLAS (made by Fukuvi Chemical Industry Co. Ltd., Fukui, Japan) solid state track detector (hereinafter referred to as STD) with dimensions of

Figure 2. Polymer composite irradiation set up using a synchrotron (red arrow shows the proton beam outgoing direction from the synchrotron channel), where: *1* — synchrotron, *2* — 4 mm aluminum shutter, *3* — water absorber (was not used for this experiment), *4* — „PILLE-MKS" sensor and passive TLD and STD assembly, *5* — polymer composite.

25×25 mm and a thickness of 0.9 mm, with a linear energy transfer (hereinafter referred to as LET) recording threshold of 10 keV/μm (H_2O), which corresponds, for example, to proton energy $5 \ldots 10$ MeV (protons with energy higher than the specified one do not form any tracks in the STD substance, however, they may participate in nuclear fragmentation acts resulting in formation secondary particles with LET higher than the threshold) [19].

After irradiation, the detectors were etched and flushed, and then their surface was scanned in semi-automatic mode using SEIKO® FlexSCOPE FSP-1000 modified semi-automatic optical tomographic microscope [20].

Charged particle track parameters were recognized using SEIKO® PitFit v. 2.0 specialized digital image recognition and analysis software.

Output test data files were imported into MATLAB® and processed statistically. To determine the relative etching rate V, a so-called „classical" method was used for each track when the major axis A and minor axis B of the ingoing ellipse are the input parameters [21]:

$$V = \frac{V_t}{V_b} = \sqrt{\frac{16H_0^2 A^2}{(4H_0^2 - B^2)^2} + 1}. \tag{1}$$

Then the obtained etching rates were recalculated into LET using a calibration function pre-defined for this type of detector [19].

Then differential spectra of LET, absorbed and equivalent (in accordance with ICRP recommendations [22]) doses

were calculated in accordance with the standard procedure described in [23].

2.3. Test methods

Mechanical properties of the composite were measured using REM-100-A-1-1 general-purpose test machine with upper load measurement limit of 100 kN. Manufacturer — LLC „Metrotest", Republic of Bashkortostan, Neftekamsk.

Micrographs of the material were made using TESCAN MIRA 3 LMU high resolution scanning election microscope. Micrographs were made in SE mode— Everhart-Thornley secondary electron detector.

Scanning probe microscopy was carried out using „Ntegra-Aura" scanning probe microscope. Studies were carried out in constant or intermittent contact modes using „Ntegra-Aura" (NT-MDT, Zelenograd, Russia) instrument with commercial Si or SiN cantilevers (NSG01, NT-MDT, Russia) in atmosphere and low vacuum conditions. Surface roughness analysis was performed on the $100 \times 100 \mu$m area.

Microhardness of samples was measured by the static cone indentation method using the Vickers diamond pyramid, followed by the measurement of diagonal lengths on the restored indentation and conversion of diagonal lengths into Vickers hardness (HV) using Nexus 4504-IMP hardness tester.

The modulus of elasticity was calculated using equation (2) and PULSAR-1.2 ultrasound propagation time meter

$$E = \frac{\gamma V^2}{0.95} \cdot 10^3, \tag{2}$$

where E is the modulus of elasticity, Pa, V is the ultrasound speed value, m/s, γ is the bulk density, g/cm³.

Contact angle of wetting was assessed using Krüss DSA 30 (KrüssGmbH, Germany) instrument.

Grain size of powder materials was measured by the grain size analysis method using Analysette 22 NanoTec plus laser light scattering particle size analyzer.

3. Findings and discussion

3.1. Study of physical and mechanical properties of polymer composite

To study the effect of filler particle sizes on the polymer composite structure, the grain size analysis of powder materials was carried out. Particle size distribution of two different fillers is shown in Figure 3, *a, b*.

Grain size analysis data review has shown that particle sizes of the first filler are in the range from 0.08μm to 25.9μm, modal particle diameter is 0.09μm, and specific particle surface is 106489 cm²/cm³. The second filler has particle sizes in the range from 0.09μm to 24.7μm, a modal particle diameter of 10.31μm and a specific particle surface of 108 268 cm²/cm³.
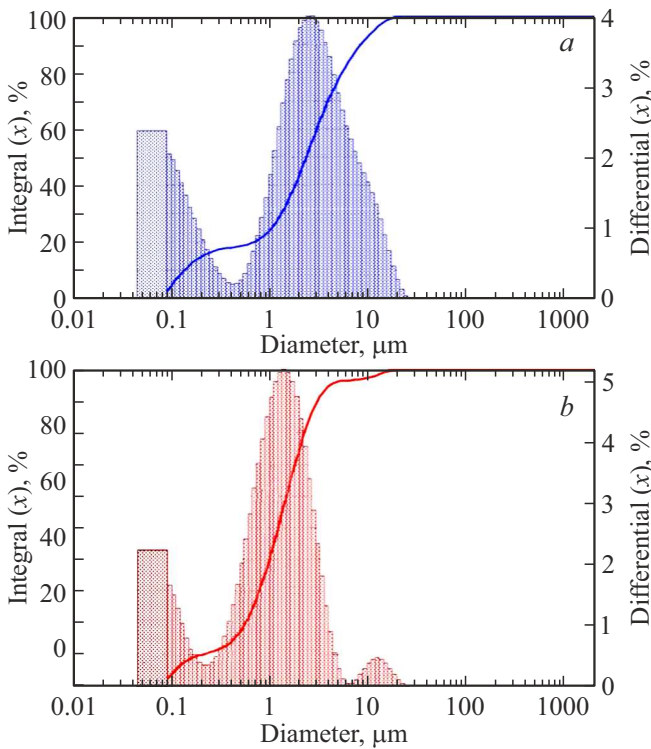
Figure 3. Grain size of powders of the first (*a*) and second (*b*) fillers.

For microstructural analysis of the polymer composite surface, microphotographs of the surface were made in SE mode — the Everhart-Thornley secondary electron detector, see Figure 4.

The polymer composite surface microphotographs show roughness with $15\,\mu$m cavities, whose size may depend on

Table 2. Vickers hardness of polymer composite

Measurement point	Vickers hardness, HV (at 200 g)
Outer surface	5.03
Cross-section	4.93

the filler particle sizes which is confirmed by particle size distribution analysis of fillers, scanning probe microscopy was carried out for more detailed investigation and is shown in Figure 5.

Roughness values measured by the scanning probe microscopy are as follows: mean roughness (Sa) $2.17\,\mu$m; Sz — ten point height $7.82\,\mu$m; Sq — rms roughness $2.74\,\mu$m, maximum roughness $14.71\,\mu$m.

Fillers are evenly distributed throughout the material, there are no large agglomerate particles, therefore physical, mechanical and radiation protection properties may be expected to be identical in various test points.

Then to study polymer composite hardness, microhardness was measured and converted into Vickers hardness.

Microhardness tester indentation image in microhardness measurement at 200 g is shown in Figure 6.

Microhardness measurements are shown in Table 2.

As shown in Table 2, Vickers hardness on the polymer composite surface almost coincides with that in the volume. A small difference of 0.10 HV may be explained by the damage of material layer bonding during cutting.

For more detailed study of this issue, ultimate bending strength testing was performed on $50 \times 10 \times 7$ mm polymer composite samples by the 3-point bending method. The ultimate bending strength test curve is shown in Figure 7.
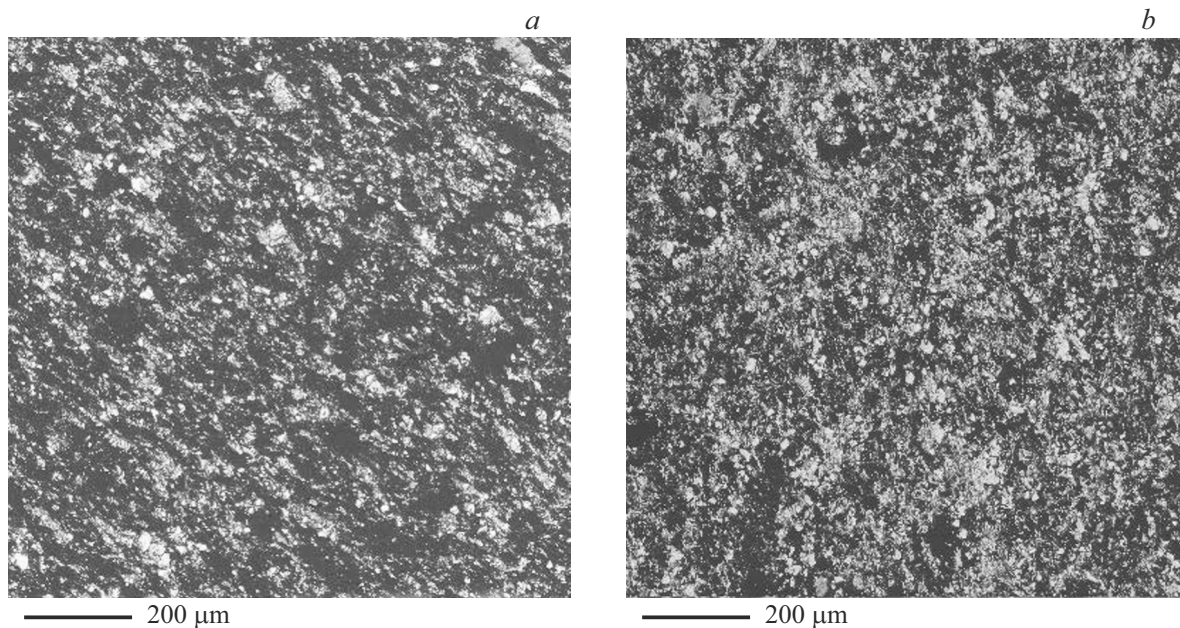

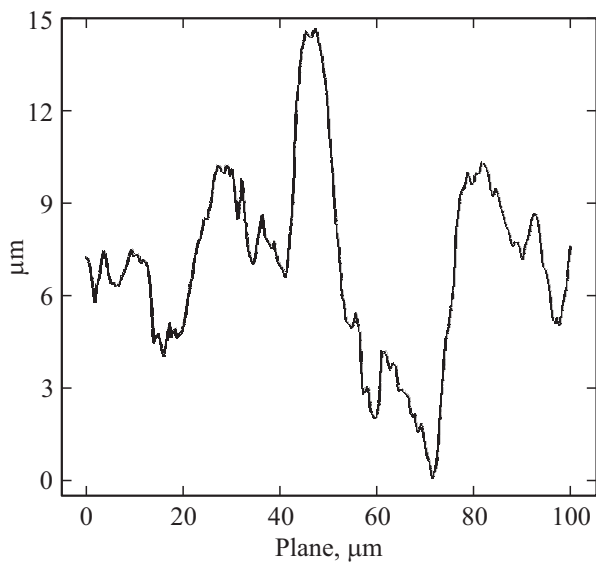**Figure 4.** Microphotographs of polymer composite surface: *a* — outer surface; *b* — cross-section.

Figure 5. 2-D AFM image of the polymer composite surface.

Table 3. Modulus of elasticity of polymer composite

Polymer composite measurements		
Point 1		
	Measurement 1	Measurement 2	Measurement 3
V, m/s	2472	2459	2468
V_{av}, m/s		2466.33	
T	66.77	66.95	66.82
T_{av}		66.84	
E, GPa		26.25	
Point 2		
	Measurement 1	Measurement 2	Measurement 3
V, m/s	2437	2429	2426
V_{av}, m/s		2430.66	
T	67.75	67.89	67.79
T_{av}		67.81	
E, GPa		25.50	
Point 3		
	Measurement 1	Measurement 2	Measurement 3
V, m/s	2459	2437	2426
V_{av}, m/s		2440.66	
T	67.89	66.95	66.77
T_{av}		67.20	
E, GPa		25.71	
M, g		253.7	

Five polymer composite samples were tested, the minimum ultimate bending strength was equal to 17.1 MPa (maximum load 315 N) and the maximum ultimate bending strength was 20.8 MPa (maximum load 414 N), mean ultimate bending strength was 19 MPa (mean maximum load 341 N). Maximum strain varies from 1.2 mm to 1.3 mm.

Modulus of elasticity of the polymer composite was also calculated by the ultrasonic test method using equation (2). The ultrasonic method is based on the dependence of ultrasonic vibration (wave) propagation speed in materials on elasticity of materials, see Table 3, where point *1* is the measurement on the top of the container, point *2* is the measurement in the middle of the container, point *3* is the measurement on the bottom of the container.

Stable modulus of elasticity suggest that the container has rather uniform structure and no significant internal defects were detected.

To study the polymer composite surface properties, contact angle of wetting was investigated. Figure 8 shows the images of non-movable distilled water and diiodomethane droplets on the polymer composite surface.
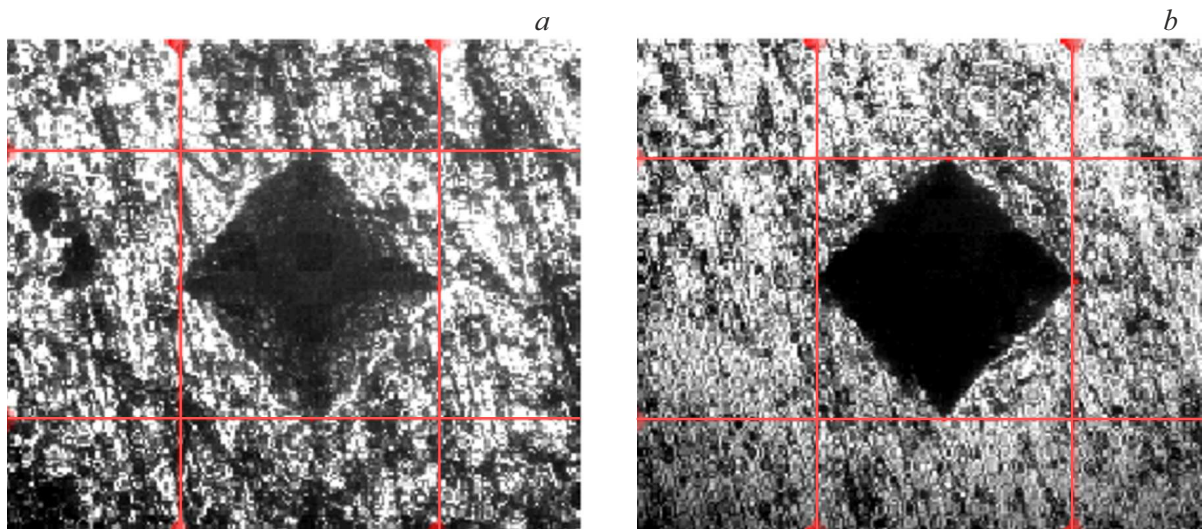

Figure 6. Microhardness tester indentation image in microhardness measurement at 200 g: *a* — outer surface; *b* — cross-section.

Table 4. Physical and mechanical properties of the polymer composite

Parameter	Value
Density, g/cm³	4.05
Vickers microhardness HV/1 (load 200 g), HV	5.03
Ultimate bending strength, MPa	19
Modulus of elasticity, GPa	25.82
Contact angle of wetting with water, °	100.98 ± 2.60
Contact angle of wetting with diiodomethane, °	57.50 ± 8.33
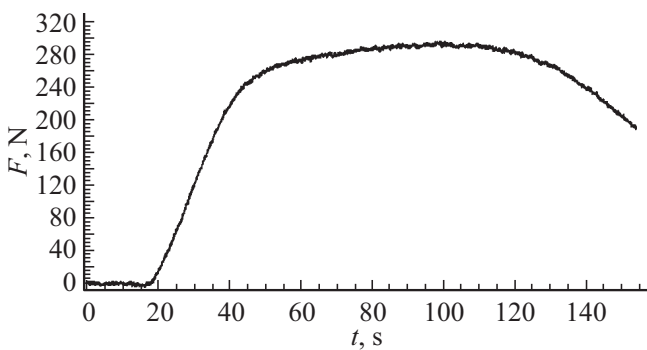
Figure 7. Applied load vs. time curves for polymer composite sample.

Measurements of the contact angle of wetting have shown that the polymer composite surface is well wetted with diiodomethane (52.1° and 54.4°), and is not wetted with water (102.5° and 103.4°).

Diiodomethane was chosen for measurements of the contact angle of wetting on the composite surface, because it is a nonpolar solvent, it is needed to assess the contribution of polar and dispersion (nonpolar) components to the free surface energy that will be calculated using the Owens–Wendt–Rabel-Kaelble (OWRK).

Physical and mechanical properties of the polymer composite are listed in Table 4.

Thus it is shown that the polymer composite has good physical and mechanical properties. Then protective properties of this composite against gamma and proton irradiation were tested.

3.2. Study of gamma protective properties of the polymer composite

Gamma protective properties of the polymer composite were evaluated theoretically according to the atomic analysis of the polymer composite (Table 1). Gamma radiation attenuation is caused by photoeffect, Compton effect and electron-positron pair effect.

Equation for calculation of gamma quanta flux attenuation coefficient due to photoeffect for the polymer composite

$$\mu_f = 4\pi r_e^2 \alpha^4 N_a \left(\rho_{Bi} \frac{Z_{Bi}^5}{A_{Bi}} + \rho_O \frac{Z_O^5}{A_O} + \rho_C \frac{Z_C^5}{A_C} \right.$$
$$\left. + \rho_F \frac{Z_F^5}{A_F} + \rho_W \frac{Z_W^5}{A_W} \right) G_{fot}(E), \qquad (3)$$

where ρ_i is the density of the particular element, Z_i is the particular element No., A_i is the atomic weight of the particular element, N_A is Avogadro's number equal to $6.02 \cdot 10^{23}$, $r_e = e^2/m_e c^2 = 2.8 \cdot 10^{-13}$ cm is the classical electron radius, $\alpha = 1/137$ is the fine structure constant, G_{fpt} is the photoeffect process effect on the atom [24].

Calculation of the gamma quanta flux attenuation coefficient due to the Compton effect through the polymer composite is represented by the equation

$$\mu_K = N_a \left(\rho_{Bi} \frac{Z_{Bi}}{A_{Bi}} + \rho_O \frac{Z_O}{A_O} + \rho_C \frac{Z_C}{A_C} + \rho_F \frac{Z_F}{A_F} + \rho_W \frac{Z_W}{A_W} \right) \sigma_K, \qquad (4)$$

where σ_K are the Compton gamma quantum scattering process cross-sections on the electron [24].

γ-quanta flux attenuation coefficient due to formation of electron-positron pairs in the polymer composite

$$\mu_p = r_e^2 \alpha N_a \left(\frac{\rho_{Bi}}{A_{Bi}} Z_{Bi}(Z_{Bi} + 1) + \frac{\rho_O}{A_O} Z_O(Z_O + 1) \right.$$
$$+ \frac{\rho_C}{A_C} Z_C(Z_C + 1) + \frac{\rho_F}{A_F} Z_F(Z_F + 1)$$
$$\left. + \frac{\rho_W}{A_W} Z_W(Z_W + 1) \right) \left[\frac{28}{9} \ln(2\varepsilon) - \frac{218}{27} \right], \qquad (5)$$

where $\varepsilon = E/m_e c^2$.

Total γ-quantum attenuation coefficient in the polymer composite consists of the sum of attenuation coefficient from each process

$$\mu = \mu_f + \mu_k + \mu_p p. \qquad (6)$$

For visibility, the polymer composite measurements (hereinafter referred to as compound 2) will be compared with the measurements of the most commonly used polymers such as PTFE (hereinafter referred to as compound 1) and PE (hereinafter referred to as compound 3) whose density is 2.2 and 1.0 g/cm³, respectively.

The curve of γ-quanta attenuation coefficient vs. energy is shown in Figure 9.

The curve shows that the γ-quanta attenuation coefficient throughout the energy range is higher by a factor of 2 or more than for the reference polymers. Special focus shall be made on the energy range from 0.01 to 0.5 MeV where it can be seen that the offered polymers little if any attenuate gamma quanta at low energies compared with the offered polymer composite. With increasing energy, gradual convergence and alignment of curves occurs, with approximate stabilization near 2−3 MeV.
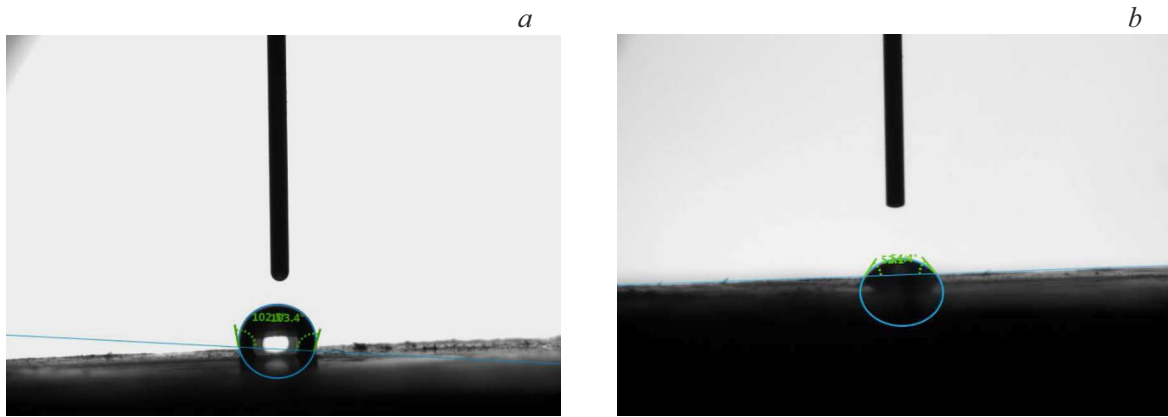
Figure 8. Images of non-moving droplet on the polymer composite surface: *a* — water, *b* — diiodomethane.
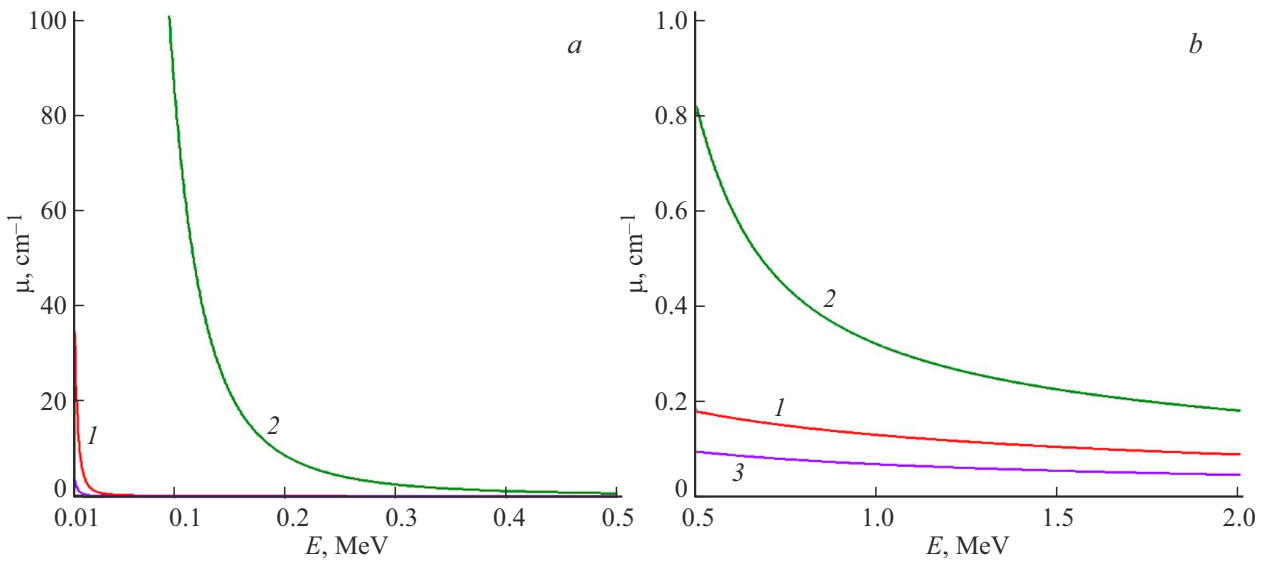

Figure 9. γ-quanta attenuation coefficient vs. energy: *a* — 0.01 to 0.5 MeV; *b* — 0.5 to 2 MeV (*1* — PTFE, *2* — polymer composite, *3* — PE).
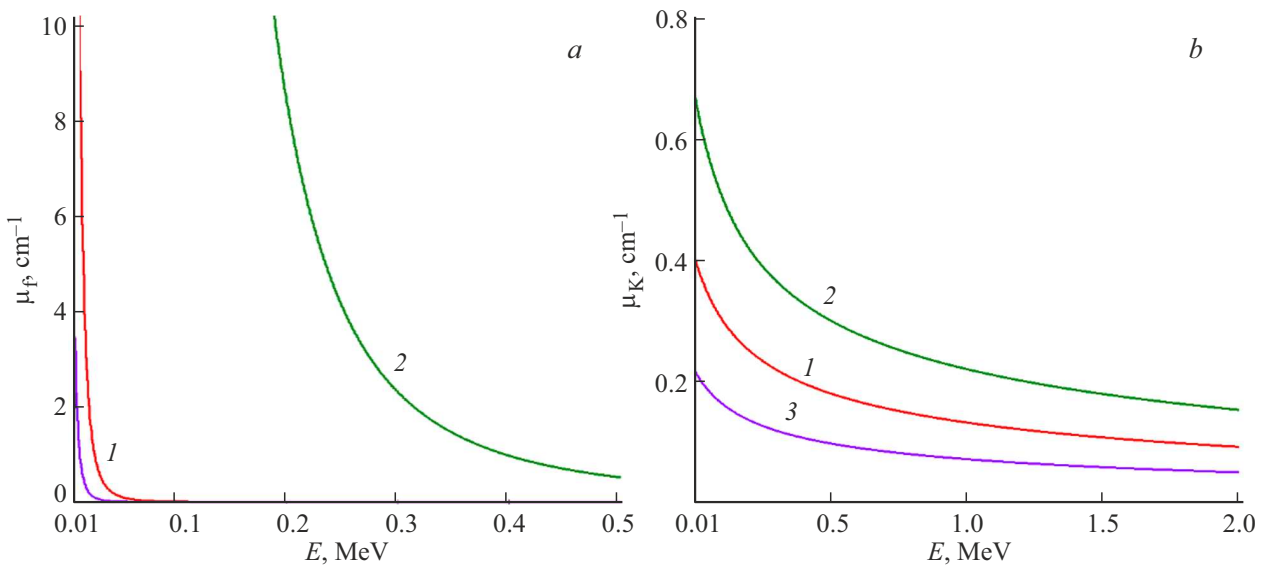

Figure 10. Contribution of photoeffect (μ_f) and Compton effect (μ_k) to the total attenuation coefficient in the polymer composite.

Table 5. Linear attenuation coefficient of gamma quanta

	Linear attenuation coefficient, cm^{-1}			
	$E = 0.08\,MeV$	$E = 0.570\,MeV$	$E = 0.662\,MeV$	$E = 1.252\,MeV$
PTFE (compound 1)	$\mu = 0.407$	$\mu = 0.171$	$\mu = 0.16$	$\mu = 0.118$
Polymer composite (compound 2)	$\mu = 490.616$	$\mu = 0.647$	$\mu = 0.516$	$\mu = 0.261$
PE (compound 3)	$\mu = 0.191$	$\mu = 0.092$	$\mu = 0.086$	$\mu = 0.064$
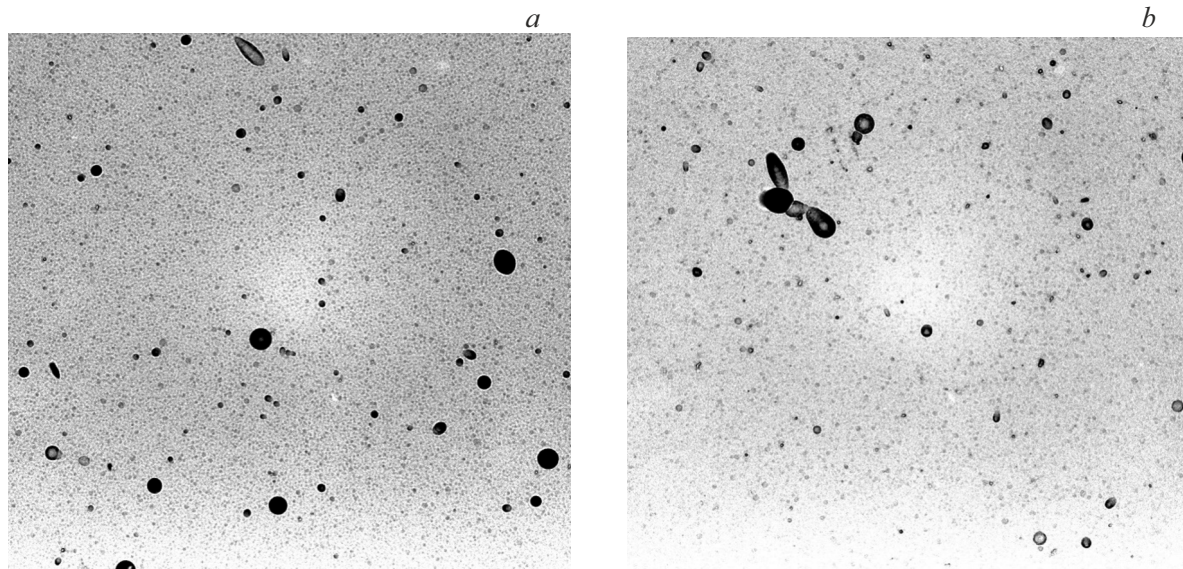
Figure 11. Secondary charged particle tracks formed in the STD volume after exposure to the proton beam behind the local protection: $4\,mm\,Al + 5\,cm$ boronated PE (*a*), $4\,mm\,Al + 1\,cm$ polymer composite (*b*).

Linear gamma quanta attenuation coefficient values in Table 5.

At low energies, the reference polymers (compound 1 and compound 3) are more than 490 times less effective (at 0.08 MeV) compared with the offered polymer composite (Table 5). But with increasing energy, the difference reduces, but is still considerably higher than that of the reference polymers.

Then to evaluate the contribution of the photoeffect and Compton effect to the total gamma quanta attenuation coefficient, curves of gamma quanta attenuation vs. energy were plotted for each effect individually in the polymer composite and are shown in Figure 10. Calculated contribution of the electron-positron pair creation to the total gamma quanta attenuation coefficient in the specified energy range is next to zero (and is not available at all at energies lower than 1.022 MeV), therefore it is not shown in the figure.

The main contribution of the photoeffect to the gamma quanta attenuation falls on the energy range from 0.01 to 0.5 MeV, almost without contribution for compound 3 and to a lesser extent for compound 1. At 0.5 MeV, the photoeffect and Compton effect contribution for compounds 1 and 2 is approximately similar, then the main attenuation is caused by the Compton effect. Such gamma protective property measurements are explained by high density of the polymer composite due to high concentration of Bi in the compound uniformly distributed throughout the volume.

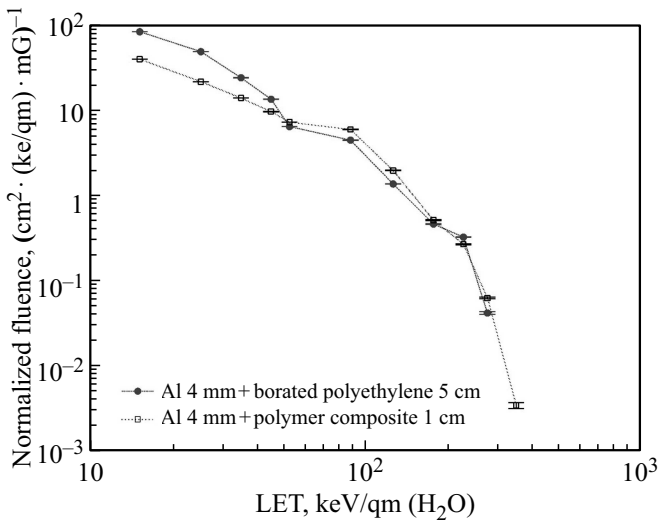## 4. Experimental study on exposure of the polymer composite to proton beam

After exposure to the proton beam behind two local protection assemblies ($4\,mm\,Al + 5\,cm$ boronated (density $0.94\,g/cm^3$) PE, $4\,mm\,Al + 1\,cm$ polymer composite), the detectors were subjected to etching. Figure 11 shows the detector surfaces after etching and flushing. Area of each image is $0.044\,mm^2$.

The provided images show that the number of tracks behind the boronated PE protection is much higher than behind the polymer composite protection. While the local polymer composite protection thickness is 5 times lower than that of the boronated PE.

Then LET spectra were measured. The measured LET spectra normalized to the ingoing primary (proton) radiation dose (according to the TLD data) as recommended in [19] are shown in Figure 12.

Table 6. Calculated absorbed and equivalent secondary particle doses behind different local protections

Local protection material	D_{ETD}, mGy (H_2O)	Contribution to the total absorbed dose, %	H_{ETD}, mSv (H_2O)	Contribution to the total equivalent dose, %
4 mm Al + 5 cm boronated PE	17 ± 1	11%	239 ± 7	9%
4 mm Al + 1 cm polymer composite	15 ± 1	63%	261 ± 8	64%

Figure 12. LET spectra of secondary charged particles measured using STD behind two local protection assemblies.

The Figure shows that considerable decrease in the secondary particle fluence is observed behind the local protection (4 mm Al + 1 cm polymer composite) compared with local protection (4 mm Al + 5 cm boronated PE), in the LET region < 40 keV/μm (H_2O), which may be attributed to a lower yield of neutrons with energies lower than 0.5 . . . 1 MeV that are responsible for formation of single recoil proton tracks [25]. At the same time, an increase in fluence of heavy densely ionizing fragments with LET from 50 to 200 keV/μm (H_2O) is observed and there are fragments with LET > 250 keV/μm (H_2O) that are not observed in the spectrum with protection (4 mm Al + 5 cm boronated PE). Both primary protons with energies higher than 50 MeV (that have passed the local protection and interacted with the STD substance) and secondary neutrons with energies about 10 . . . 20 MeV (formed in the local protection and interacting with the STD substance) are responsible for formation of this portion of spectrum [26]. From radiobiological prospect, particle with LET from 80 to 300 keV/μm (H_2O) have the highest relative biological effectiveness (RBE) [27], maximum decrease in the particle contribution in this LET spectral range is the most important.

Calculated absorbed dose D_{ETD} and equivalent dose H_{ETD} (according to the STD data) are shown in Table 6. Contribution of absorbed STD dose D_{ETD} and equivalent

STD dose H_{ETD} to the total dose is defined as the ratio of the appropriate value to the total value defined as the sum of STD dose (secondary component and TLD dose (primary component) [28].

As shown in Table 6, adsorbed doses D_{ETD} in both cases are almost the same within the measurement accuracy. At the same time, equivalent dose H_{ETD} is higher behind a heavier protection (polymer composite) due to the presence of heavy densely ionizing nuclear fragmentation products. Generally, both equivalent doses H_{ETD} agree within 20 . . . 30% allowable for various types of dosimetric measurements, therefore these measurements may not be treated as consistently different from each other.

Increasing yield of heavier nucleus fragments *C*, *O* may be attributed both to an decrease in bombarding proton energy (total cross-section of nuclear interaction grows with decreasing energy from 160 MeV up to 50 MeV) [29,30] and to an increase in the high-energy neutron yield (10 . . . 20 MeV) [25,26] from the polymer composite material. Contributions of the absorbed and equivalent STD doses listed in the Table are twice as high as those measured earlier on 157 MeV proton beams without using the local protection [31]. This may imply the influence of the secondary neutron component responsible for additional generation of nuclear fragments in the STD material.

Thus, the reference measurements of LET spectra and secondary nuclear fragment doses behind two types of local protection (4 mm AL + 1 cm polymer composite) and (4 mm Al + 5 cm boronated PE) demonstrate approximately the same protection performance of the chosen materials. Compared with (4 mm Al + 5 cm boronated PE), the polymer composite suppresses the secondary particle yield in the STD material with LET < 40 keV/μm (H_2O) due to the decrease in proton energy, at the same time the yield of nuclear fragments with LET from 50 to 200 keV/μm and more than 250 keV/μm (H_2O) having the maximum biological effectiveness increases. In terms of integral absorbed and equivalent doses accumulated in the STD material (simulating a soft biological tissue), no significant difference in the use of the two types of protection materials is observed. But protection thickness is important, because the local polymer composite protection in 5 times thinner than the PE protection.

Combination of the polymer composite with the boronated PE in the form of a multilayer assembly is possible for protection throughout the energy range due to taking advantages of both materials.

5. Conclusion

Availability of a polymer composite material with high physical and mechanical properties was established: density — $4.05\,\mathrm{g/cm^3}$, Vickers microhardness at a load of $200\,\mathrm{g}$ — 5.03 HV, modulus of elasticity — 25.82 GPa.

The calculation of the gamma quanta attenuation coefficient has demonstrated high gamma radiation protection performance of the polymer composite: at $E = 0.08\,\mathrm{MeV}$, μ is equal to $490.62\,\mathrm{cm^{-1}}$, and at $E = 1.252\,\mathrm{MeV}$, the coefficient is only $0.26\,\mathrm{cm^{-1}}$.

Exposure of the polymer composite to the proton beam has also shown its high radiation protection performance. When the $4\,\mathrm{mm\,Al} + 1\,\mathrm{cm}$ polymer composite assembly was exposed to proton irradiation, considerable decrease in the secondary particle fluence was found in the LET region $< 40\,\mathrm{keV}/\mu\mathrm{m}$ (H_2O), which may be attributed to a lower yield of neutrons with energies lower than $0.5\ldots1\,\mathrm{MeV}$ that are responsible for formation of single recoil proton tracks. At the same time, an increase in fluence of heavy densely ionizing fragments with LET from 50 to $200\,\mathrm{keV}/\mu\mathrm{m}$ (H_2O) was observed and there were fragments with LET $> 250\,\mathrm{keV}/\mu\mathrm{m}$ (H_2O).

The developed polymer composite may be applicable as a material for protection against cosmic radiation. Protection thickness will be the main advantage of the used protection, because the local polymer composite protection is 5 times thinner than the PE protection (most commonly used material for protection in the inhabited modules if ISS) which is important for the use of materials on board spacecraft where the effective and living space is strongly restricted.

Funding

Conflict of interest

The authors declare that they have no conflict of interest.

References

[1] Yu.G. Grigoriev, I.B. Ushakov, A.V. Shafirkin. Gigiena i sanitariya, **96** (9), 2017 (2013). (in Russian)

[2] V.M. Baranov, V.P. Katuntsev, M.V. Baranov, A.V. Shpakov, G.G. Tarasenkov. Ulyanovsky med.-biol. zhurn. **3**, 109 (2018). (in Russian).

[3] F. Horst, D. Boscolo, M. Durante, F. Luoni, C. Schuy, U. Weber. Life Sci. Space Res. (Amsterdam) **33**, 58 (2022).

[4] C. Mehner, S. Krishnan, J. Chou, M.L. Freeman, W.D. Freeman, T. Patel, M.T. Turnbull. Life Sci. Space Res. (Amsterdam) **29**, 8 (2021).

[5] S.N. Kuznetsov, V.G. Kurt, I.N. Myagkova, B.Yu. Yushkov, K.N. Kudela. Astronom.vestn. **40**, *2*, 120 (2006). (in Russian).

[6] T.P. Dachev, M.L. Litvak, E. Benton, O. Ploc, B.T. Tomov, Y.N. Matviichuk, P.G. Dimitrov, R.T. Koleva, M.M. Jordanova, N.G. Bankov, M.G. Mitev, I.G. Mitrofanov, D.V. Golovin, M.I. Mokrousov, A.B. Sanin, Vladislav.I. Tretyakov, V.A. Shurshakov, V.V. Benghin. Life Sci. Space Res. (Amsterdam) **39**, *11*, 43 (2023).

[7] A.S. Samoilov, I.B. Ushakov, V.A. Shurshakov. Ekologiya cheloveka, **26** (1), 4 (2019). (in Russian)

[8] M. Naito, H. Kitamura, M. Koike, H. Kusano, T. Kusumoto, Y. Uchihori, T. Endo, Y. Hagiwara, N. Kiyono, H. Kodama, S. Matsuo, R. Mikoshiba, Y. Takami, M. Yamanaka, H. Akiyama, W. Nishimura, S. Kodaira. Life Sci. Space Res. (Amsterdam) **31**, 71 (2021).

[9] J.M. DeWitt, E.R. Benton, Y. Uchihori, N. Yasuda, E.V. Benton, A.L. Frank. Rad. Meas. **44**, *9*, 905 (2009).

[10] C. La Tessa, S. Guetersloh, L. Heilbronn, J. Miller, L. Sihver, C. Zeitlin. Adv. Space Res. **35**, *2*, 223 (2005).

[11] C. Zeitlin, D.M. Hassler, F.A. Cucinotta, B. Ehresmann, R.F. Wimmer-Schweingruber, D.E. Brinza, S. Kang, G. Weigle, S. Böttcher, E. Böhm, S. Burmeister, J. Guo, J. Köhler, C. Martin, A. Posner, S. Rafkin, G. Reitz. Science **340**, *6136*, 1080 (2013).

[12] S. Kodaira, R.V. Tolochek, I. Ambrozova, H. Kawashima, N. Yasuda, M. Kurano, H. Kitamura, Y. Uchihori, I. Kobayashi, H. Hakamada, A. Suzuki, I.S. Kartsev, E.N. Yarmanova, I.V. Nikolaev, V.A. Shurshakov. Adv. Space Res. **53**, *1*, 1 (2014).

[13] N.I. Cherkashina, V.I. Pavlenko, A.V. Noskov, N.I. Novosadov, E.S. Samoilova. Acta Astronaut. **170**, 499 (2020).

[14] S. Laurenzi, G. de Zanet, M.G. Santonicola. Acta Astronaut. **170**, 530 (2020).

[15] L. Pernigoni, U. Lafont, A.M. Grande. Acta Astronaut. **210**, 627 (2023).

[16] B. Liu, Y. Gu, Y. Liu, S. Wang, M. Li. Composites A **168**, 107483 (2023).

[17] M. Naito, S. Kodaira, R. Ogawara, K. Tobita, Y. Someya, T. Kusumoto, H. Kusano, H. Kitamura, M. Koike, Y. Uchihori, M. Yamanaka, R. Mikoshiba, T. Endo, N. Kiyono, Y. Hagiwara, H. Kodama, S. Matsuo, Y. Takami, T. Sato, S. Orimo. Life Sci. Space. Res. (Amsterdam) **26**, 69 (2020).

[18] Patent na izobretenie RF No 2748157, MPK — 2017.01 G21F 1/12 (in Russian). V.I. Pavlenko, A.N. Shkaplerov, A.A. Kuritsyn, N.I. Tcherkashina, E.V. Popova, R.N. Yastrebinsky. Polimernyi nanokompozit dlya zashchity ot kosmicheskogo vozdeistviya i sposob ego polucheniya. Zayaviteli i patentoobladateli: Belgorodsky gos.tekhnol.un-t im. V.G. Shukhova i Nauchno issledovatel'skyi tsentr podgotovki kosmonavtov im. Yu.A. Gagarina. Zayavka №. 2020134472. Zayavleno: 20.10.2020. Opublikovano: 20.05.2021, Byul. 14. (in Russian).

[19] S. Kodaira, K. Morishige, H. Kawashima, H. Kitamura, M. Kurano, N. Hasebe, Y. Koguchi, W. Shinozaki, K. Ogura. Nucl. Instrum. Meth. Phys. Res. B **383**, 129 (2016).

[20] N. Yasuda, K. Namiki, Y. Honma, Y. Umeshima, Y. Marumo, H. Ishii, E.R. Benton. Rad. Meas. **40**, *2−6*, 311 (2005).

[21] D. Nikezic, K. Yu. Mater. Sci. Eng. R **46**, *3−5*, 51 (2004).

[22] ICRP, 1991. 1990 Recommendations of the International Commission on Radiological Protection. ICRP Publication 60. Ann ICRP **22**, *1−3*, 1 (1991).

[23] J.K. Pálfalvi. Rad. Meas. **44**, *9−10*, 724 (2009).

[24] A.L. Bespalov. Izd-vo „Deltaplan", Tomsk (2006).

[25] V.V. Kushin. Rad. Prot. Dosimetry **141**, *2*, 199 (2010).

[26] H. Tawara, K. Eda, T. Sanami, S. Sasaki, K. Takahashi, R. Sonkawade, A. Nagamatsu, K. Kitajo, H. Kumagai, T. Doke. Jpn. J. Appl. Phys. **47**, *3*, 1726 (2008).

[27] T. Friedrich, U. Scholz, T. ElsaSser, M. Durante, M. Scholz. J. Rad. Res. **54**, *3*, 494 (2013).

[28] K.O. Inozemtsev, S. Kodaira, T. Kusumoto, H. Kitamura, A. Strádi, J. Szabó, I. Ambrožová, V.A. Shurshakov. Rad. Meas. **140**, 106505 (2021).

[29] M. Durante, F.A. Cucinotta. Rev. Mod. Phys. **83**, *4*, 1245 (2011).

[30] F.A. Cucinotta, J.W. Wilson, J.L. Shinn, F.F. Badavi, G.D. Badhwar. Rad. Meas. **26**, *6*, 923 (1996).

[31] S. Kodaira, H. Kitamura, M. Kurano, H. Kawashima, E.R. Benton. Sci. Rep. **9**, *1*, 3708 (2019).

Translated by E.Ilinskaya